J Adv Ceram

Research Article

High-*Q* enstatite microwave/terahertz dielectric ceramics modulated by phase transition and lattice distortion

Yutian Lu, Weijia Guo✉, Chongyang Zhang, Hui Zhang, Zhenxing Yue✉

Cite this article: Lu Y, Guo W, Zhang C, et al. *J Adv Ceram* 2025, **14**(4): 9221053. https://doi.org/10.26599/JAC.2025.9221053

ABSTRACT: The rapid development of fifth-/sixth-generation telecommunication technologies has increased the demand for silicate ceramic materials with low permittivity and low dielectric loss. However, few silicate ceramics with ultrahigh $Q\times f$ values (≥ 200,000 GHz) have been developed to date. In this study, a slight substitution of Ge^{4+} ions in $MgSi_{1-x}Ge_xO_3$ (MSG*x*, x = 0 to 0.6) ceramics caused a phase transition from clinoenstatite (x = 0) to orthoenstatite (x = 0.2), and the $Q\times f$ value increased from 70,600 GHz to 148,800 GHz. Following the phase transition, the cations change from a "compressed" state to a "rattle" state, and the lattice distortion continues to rise with x, resulting in the optimal microwave dielectric properties (ε_r = 7.21, $Q\times f$ = 259,300 GHz) of the $MgSi_{0.5}Ge_{0.5}O_3$ ceramics. Significant discrepancies in the dielectric properties are found in the microwave and terahertz bands. There is an anomalous increase in ε_r and a decrease in the $Q\times f$ value in the terahertz band, which is due to the change in polar phonon modes revealed by the terahertz time-domain spectra. Consequently, $MgSi_{0.7}Ge_{0.3}O_3$ ceramics display superior dielectric properties, with ε_r = 7.02, $Q\times f$ = 191,300 GHz in the terahertz band. These novel materials have the potential to serve as promising dielectric materials for future microwave or terahertz mobile communication systems.

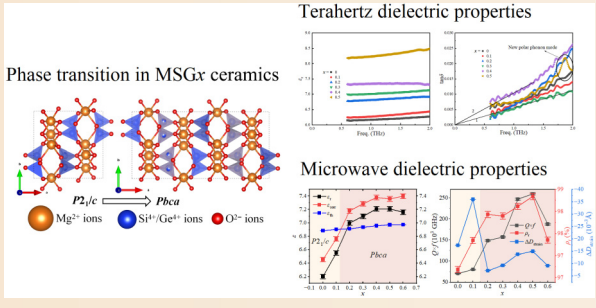

KEYWORDS: microwave dielectric property; terahertz spectroscopy; enstatite; low dielectric loss; low permittivity

1 Introduction

The rapid evolution of fifth-/sixth-generation (5G/6G) communication technologies in recent years has led to successful deployment in both communication test platforms and commercial networks [1,2]. This progress has drawn considerable attention to communication systems spanning from microwave to terahertz bands, offering the potential for greater available bandwidth, faster data transmission speeds, and reduced transmission latency [3], which are particularly beneficial in applications such as autonomous driving, the Internet of Things (IoT), and wireless communication [4]. However, these advancements place greater performance demands on the raw materials used in communication systems, particularly for lower relative permittivity (ε_r), higher $Q\times f$ (where $Q = 1/\tan\delta$, and f is the resonant frequency) values, and near-zero resonant frequency temperature coefficients (τ_f) [5–7]. Currently commercialized low-ε_r materials, such as the Al_2O_3/glass [8] and $CaO–B_2O_3–SiO_2$ glass [9] systems, may fall short due to their potentially high losses at higher frequencies. Therefore, the development of novel high-*Q* microwave/terahertz dielectric ceramics is essential.

Silicates, whose excellent performance is closely linked to their crystal structure, have long been regarded as highly promising dielectric materials for millimeter-wave applications [10]. The fundamental structural unit of silicates, the $[SiO_4]$ tetrahedron, consists predominantly of covalent bonds, with a proportion (55%) significantly greater than that in other materials, such as aluminates and titanates [11]. This high covalency contributes to reduced ionic polarization and stable crystal structures, resulting in superior dielectric properties in the microwave band, including low ε_r and high $Q\times f$ values. Silicates are categorized into island [12], chain [13], ring [14], and other structural types. Notably, silicates with high $Q\times f$ values (≥ 200,000 GHz) are often those with island frameworks, although the reasons for this are not yet fully understood [10]. Preliminary experimental results on diopside suggest that distortions within the silicate framework positively affect the $Q\times f$ value of ceramics [15]. Further study is indeed needed to clarify the relationship between silicate frameworks and dielectric properties and to develop high-*Q* ceramic values in other framework silicates.

To enable applications at higher frequencies, it is important to assess the dielectric properties of ceramics in the millimeter- and terahertz bands. However, the correlation between the dielectric properties in the microwave and terahertz bands, particularly with respect to the $Q\times f$ value, remains unclear. In some systems, the $Q\times f$ value in the microwave band is lower than that in the

State Key Laboratory of New Ceramics and Fine Processing, School of Materials Science and Engineering, Tsinghua University, Beijing 100084, China.

✉ Corresponding authors. E-mail: W. Guo, guoweijia0315@163.com; Z. Yue, yuezhx@mail.tsinghua.edu.cn

Received: December 13, 2024; Revised: February 6, 2025; Accepted: February 24, 2025

terahertz band, whereas in others, the opposite trend is observed [16,17]. This variability has been attributed to factors such as the sintering process [18], dielectric relaxation in the microwave band due to defects [19], and the influence of polar phonon modes in the terahertz band [20]. Generally, terahertz dielectric properties represent "intrinsic losses" that are closely related to the crystal structure. However, in silicates, this relationship has rarely been investigated, which requires broader studies.

Enstatite is a typical pyroxene ($M2M1T_2O_6$), with Mg^{2+} occupying the M1 and M2 sites and Si^{4+} in the T site. Its crystal structure has been extensively studied in terms of mineralogy, revealing a series of complex phase transitions [21–23], whereas studies have focused on the microwave dielectric properties [24–27]. Given that phase transitions in enstatite ceramics are often associated with distortions in the tetrahedra chain as the temperature increases, substituting Si^{4+} with Ge^{4+} also induces phase transitions in enstatite [28]. Investigating these phase transitions and the related dielectric properties could deepen the understanding of the relationship between silicate frameworks and dielectric behavior, hence supporting the development of new high-performance microwave and terahertz dielectric ceramics.

In this study, we substituted Ge^{4+} for Si^{4+} in $MgSiO_3$, compared the dielectric properties in the microwave and terahertz bands, and discussed the relationships among the crystal structure, microstructure, and dielectric properties.

2 Experimental

The ceramics were prepared via the conventional solid-state method. MgO (99.99%, Aladdin), SiO_2 (99.99%, Aladdin) and GeO_2 (99.99%, Aladdin) were used as the raw materials. All powders above were weighed according to the stoichiometric ratios of $MgSi_{1-x}Ge_xO_3$ (MSG*x*, x = 0, 0.1, 0.2, 0.3, 0.4, 0.5, and 0.6), mixed in ethanol and ball milled for 4 hours with zirconium balls as the milling media. The mixtures were dried in an oven and calcined at 1300 °C for 4 h in a muffle furnace. The calcined powders were ball milled and dried again and sieved after being pelleted with a 5 wt% polyvinyl alcohol (PVA) ethanol solution. The as-prepared powders were pressed into cylinders 10 mm in diameter and 5 mm in thickness and disks of 10 and 15 mm in diameter and 1 mm in thickness under a pressure of 200 MPa. These cylinders and disks were sintered at 1400 °C for 4 h.

X-ray diffraction (XRD) using Cu Kα radiation (D8 Advance, Bruker, Germany) was used to identify the phase composition and the crystal structure of the ceramics. The Archimedes method was used to measure the bulk density. Raman spectra obtained on a high-resolution Raman spectrometer (LabRAM HR800, Horiba Jobin Yvon, France) with the existing line at 532 nm of a Nd/YAG laser were used to identify the chemical bonds in the crystals. The ^{29}Si nuclear magnetic resonance (NMR) spectra were obtained via a 600M NMR spectrometer (JNM-ECZ600R, JEOL, Japan) and recorded at Larmor frequencies of 119 MHz. Scanning electron microscopy (SEM; MERLIN VP Compact, Carl Zeiss, Germany) was used to determine the microstructure of the samples. For SEM observation, the samples were ground and polished to a mirror surface. The thermally etching process was then carried out for 30 min at a temperature of 50 °C below the sintering temperature. The grain sizes were measured via Nano Measurer software. The microwave dielectric properties, including ε_r, the $Q\times f$ value, and τ_f, were measured by a network analyzer (HP8720ES, Hewlett-Packard, Santa Rosa, USA). ε_r was obtained via the Hakki–Coleman postresonator method by exciting the TE_{011} resonant mode [29]. $Q\times f$ values were obtained by applying the $TE_{01\delta}$ mode in the cavity method [30]. τ_f was obtained in the temperature range from T_1 to T_2 (from 25 to 80 °C) and was calculated via Eq. (1):

$$\tau_f = \frac{f_2 - f_1}{f_1(T_2 - T_1)} \tag{1}$$

where f_1 and f_2 are the resonant frequencies at T_1 and T_2, respectively [31]. THz-TDSs were measured by a terahertz time-domain spectrometer system (Z3, Zomega Terahertz Co., USA). The optical and dielectric properties of the ceramics in the terahertz band were extracted via fast Fourier transform (FFT) and Eqs. (2) and (3) [32,33]:

$$\phi_s - \phi_r = \frac{(n-1)\omega d}{c} + \arctan\frac{\kappa(-n^2+1-\kappa^2)}{n(n+1)^2+(n+2)\kappa^2} \tag{2}$$

$$A_s/A_r = \frac{4\sqrt{n^2+\kappa^2}}{(n+1)^2+\kappa^2}e^{-\kappa\omega d/c} \tag{3}$$

where ϕ_s, ϕ_r, A_s, and A_r are the phases of sample and reference, and the amplitudes of sample and reference, repectively; ω, d, and c are the angular frequency, the thickness of the sample, and the velocity of light in vacuum, respectively; n and κ are the real and imaginary parts of the complex refractive indices of the sample, respectively. The absorption coefficient (α), ε_r, and tanδ were calculated from Eqs. (4)–(6):

$$\alpha = \frac{2\omega\kappa}{c} \tag{4}$$

$$\varepsilon_r = n^2 - \kappa^2 \tag{5}$$

$$\tan\delta = \frac{2n\kappa}{\varepsilon_r} \tag{6}$$

3 Results and discussion

3.1 Composition and lattice structure

The XRD patterns of the MSG*x* ceramics (x = 0–0.6), as shown in Fig. 1, were examined to elucidate their phase composition. For x = 0 and 0.1, the ceramics exhibit a clinoenstatite phase (PDF#35-0610, $P2_1/c$, monoclinic), with peak positions shifting to lower angles as x increases, indicating successful substitution of Si^{4+} (IV, 0.26 Å) with Ge^{4+} (IV, 0.39 Å) and consequent lattice expansion. Upon increasing x to 0.2, the MSG*x* ceramics transition from clinoenstatite to orthoenstatite (PDF#19-0760, *Pbca*, orthorhombic), a structure with a different *I*-beam stacking sequence: ++−− for orthoenstatite, compared with ++ … in clinoenstatite [34]. The clino–ortho transition has been reported to be related to the distortion of tetrahedral chains, which is usually induced by changes in temperature and pressure [22]. The analogous phase transition is controlled through ion substitution in the MSG*x* ceramics, whose distortion behavior is discussed in detail below. At x = 0.6, a secondary phase of forsterite (Mg_2SiO_4) appears. This may result from the decomposition of the enstatite phase at a high sintering temperature, indicating a decrease in chemical stability. Generally, the formation of a secondary phase adversely affects the dielectric properties of ceramics. Therefore, subsequent analyses will concentrate on ceramics with compositions from x = 0 to 0.5.

Rietveld refinements are conducted to further determine the lattice and chemical bond parameters of the MSG*x* ceramics.

When x = 0.6, a two-phase refinement is performed, and the results for the enstatite phase are compared with those for other compositions. The refinement plots for samples with x = 0 and 0.2 are displayed in Figs. 2(a) and 2(b) as illustrations for clinoenstatite and orthoenstatite, respectively. The fitting results for all the samples are in good agreement with the experimental patterns, as shown in Table S1 in the Electronic Supplementary Material (ESM). Enstatite is a typical chain silicate consisting of linked [SiO_4] tetrahedra that share a common oxygen atom and form a chain structure parallel to the crystallographic c-axis, as shown in Fig. 2(c). Notably, the clino–ortho transition does not disrupt the tetrahedra chain structure. Owing to the larger ionic radius of Ge^{4+}, the fitted lattice parameters (a, b, c), and unit cell volume (V) all increase smoothly with x but change abruptly at the phase transition point, as shown in Fig. 2(d) and Table S1 in the ESM.

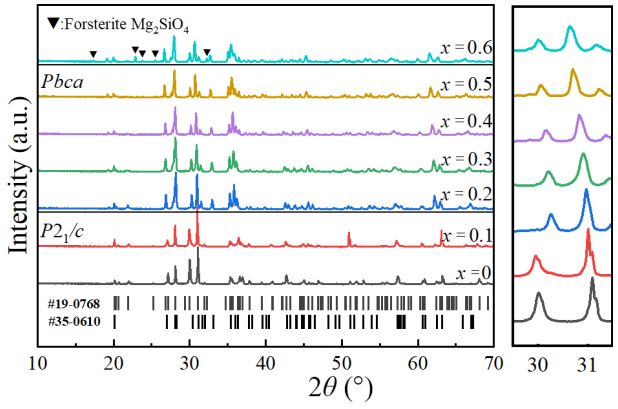

Fig. 1 XRD patterns of MSGx ceramics.

The microstructures of the MSGx ceramics were observed via SEM, and typical micrographs are shown in Fig. 3. The samples with x = 0–0.5 exhibit a dense microstructure, whereas pores begin to form alongside the secondary phase at x = 0.6. The presence of pores and secondary phases generally degrades the dielectric properties. Consequently, the dense microstructure observed in samples with x = 0–0.5 ensures that these interfering factors can be excluded in the study of their dielectric properties.

The Raman spectra of the MSGx ceramics are shown in Fig. 4. Lambruschi *et al.* [35] categorized the Raman spectra of silicates into five spectral regions:

(1) The peaks at 1100–800 cm^{-1} are attributed to the stretching modes of the Si–O_{nbr} bonds;

(2) The peaks at 800–600 cm^{-1} are attributed to Si–O_{br}–Si stretching/bending modes;

(3) The peaks at 600–450 cm^{-1} are attributed to O–Si–O vibrations;

(4) The peaks at 450–300 cm^{-1} are attributed to the motions of the cations at the M1 and M2 sites;

(5) The peaks below 300 cm^{-1} are attributed to other lattice modes;

where O_{nbr} and O_{br} are nonbridging oxygen and bridging oxygen, respectively. With the substitution of Ge^{4+}, the lattice expansion causes dilation of the [Si/GeO_4] tetrahedra. The peaks 3 and 5, corresponding to the bending vibrations of Si–O_{nbr}–Si and Si–O_{br}, shift progressively to lower wavenumbers as x increases, whereas their intensities decrease with decreasing Si–O bonds. The substitution of Ge^{4+} for Si^{4+} introduces new vibrational peaks

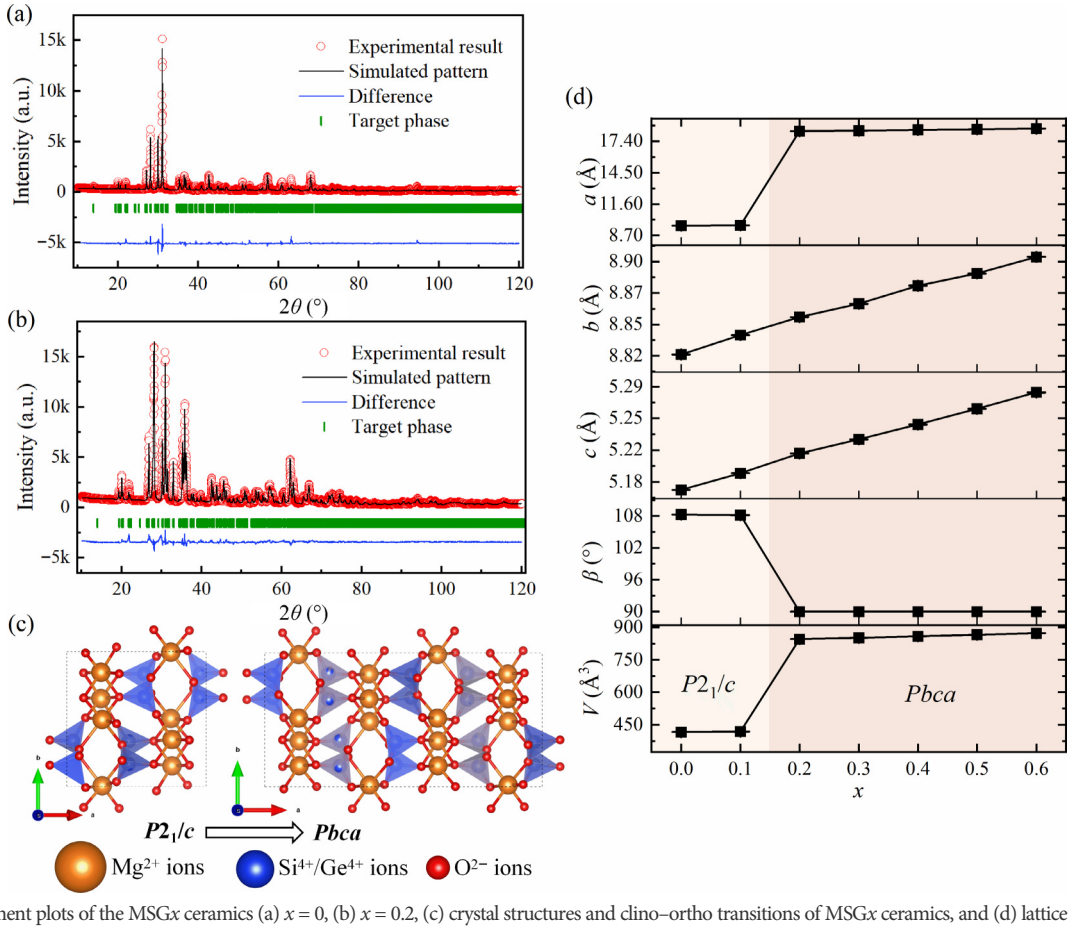

Fig. 2 Refinement plots of the MSGx ceramics (a) x = 0, (b) x = 0.2, (c) crystal structures and clino–ortho transitions of MSGx ceramics, and (d) lattice parameters and cell volumes of MSGx ceramics obtained from the refinement results.

because of the larger ionic radius and mass of Ge^{4+} ions. These peaks, including peaks 1 and 4, which correspond to the bending vibration peaks of Ge–O_{nbr}–Ge and Ge–O_{br}, respectively, appear at lower wavenumbers and exhibit a similar trend to those of the Si–O related peaks. Additionally, peak 2 is relatively unique because it corresponds to the bending vibration of Si–O_{nbr}–Ge. Although it similarly shifts to lower wavenumbers, its intensity does not change monotonically. Consistent with findings in diopside [15], this peak reaches its maximum intensity at a Si : Ge ratio of 1 : 1, or x = 0.5, indicating that the [Si/GeO_4] tetrahedra chains exhibit maximum local distortion at this composition. The Raman peaks are fitted as presented in Fig. S3 in the ESM to facilitate a more thorough analysis of the variations in the peaks.

Figure 5(a) shows the ^{29}Si NMR spectra of the MSGx ceramics, which are more sensitive to the varying environments around the Si^{4+} ions and the x-axis represents the chemical shift (δ). The spectra are fitted, and the result of x = 0.2 is presented in Fig. 5(b) as an example. All the spectra can be divided into 4 different peaks. When x = 0, the peaks 1 and 2 are inherent to the pyroxene phase and correspond to two distinct Si^{4+} sites: Si1, which is edge-sharing with [MgO_6] octahedra, and Si2, which is corner-sharing with [MgO_6] octahedra. As x increases, two additional sets of peaks, designated as 3 and 4, emerge at lower chemical shifts. Following conventions from studies on Ca-Tschermak pyroxene ($CaAl_2SiO_6$) [36,37], we define the general formula Sim[n] (m = 1, 2; n = 1, 2), where Sim ions are adjacent to n [GeO_4] tetrahedra. Thus, the peak 1 is associated with Si1[0], the peak 2 with Si1[1] and Si2[0], the peak 3 with Si1[2] and Si2[1], and the peak 4 with Si2[2]. The peak areas reflect the content of the corresponding

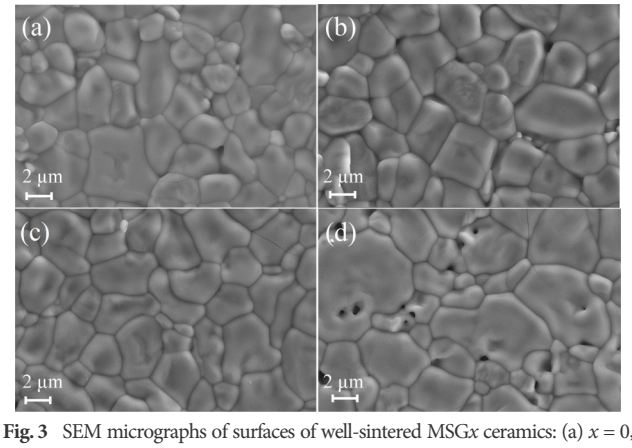

Fig. 3 SEM micrographs of surfaces of well-sintered MSGx ceramics: (a) x = 0, (b) x = 0.2, (c) x = 0.5, and (d) x = 0.6.

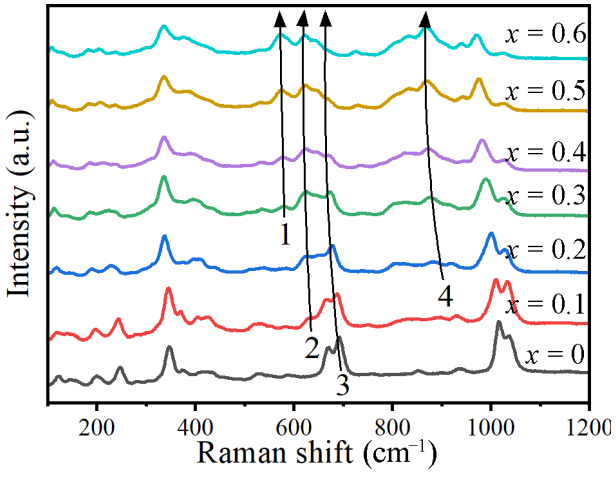

Fig. 4 Raman spectra of MSGx ceramics.

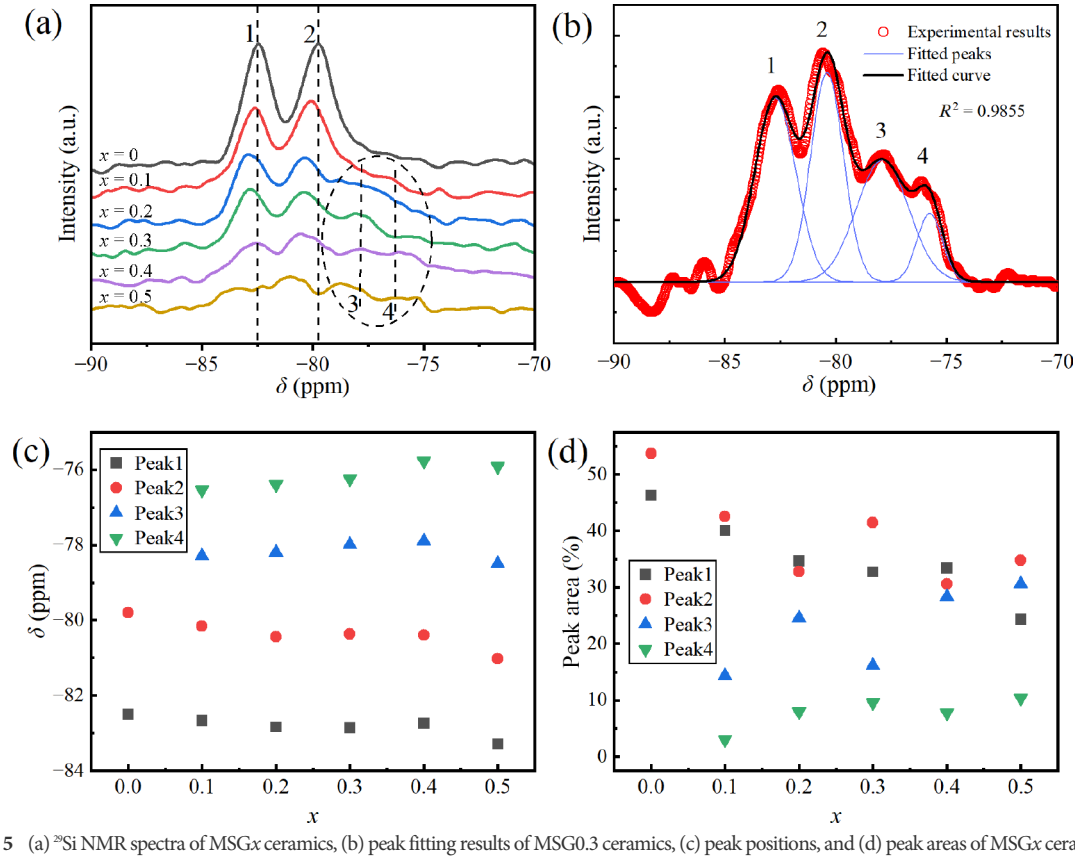

Fig. 5 (a) ^{29}Si NMR spectra of MSGx ceramics, (b) peak fitting results of MSG0.3 ceramics, (c) peak positions, and (d) peak areas of MSGx ceramics.

atom. With increasing x, the peak areas of the peaks 3 and 4 intensify, suggesting an increase in Si^{4+} ions neighboring one or two [GeO_4] tetrahedra. The peak areas of the peaks 3 and 4 reach a maximum at x = 0.5, indicating that the Si–O–Ge structure is most prevalent and that the degree of local distortion in the [Si/GeO_4] tetrahedra chain is highest at this composition.

3.2 Dielectric properties in the microwave and terahertz bands

The optical and dielectric properties of the MSGx ceramics in the terahertz band are presented in Fig. 6. Both n and ε_r increase gradually with frequency because polar phonon modes typically occur in the terahertz range. With low n and α values in the terahertz band, MSGx ceramics exhibit favorable characteristics for terahertz optics. According to classical dispersion analysis, tanδ is proportional to the angular frequency (ω) when $\omega \ll \omega_T$ (Eq. (7)):

$$\tan\delta = \frac{\varepsilon''}{\varepsilon'} \approx \frac{\gamma\omega}{\omega_T^2} \tag{7}$$

where ε' and ε'' are the real and imaginary parts of the complex dielectric constant; γ and ω_T are the damping factor and frequency of the transverse optical mode, respectively. A linear fit through the origin, with a slope proportional to γ, is used to model the tanδ–f curve of the MSGx ceramics in the terahertz band. The reciprocal of the slope represents the $Q\times f$ value in the terahertz band, as illustrated by the fitted line for x = 0.3 in Fig. 6(d). However, not all data align well with this model, such as the line fitted for x = 0.4. A new polar phonon mode emerges near 1.87 THz at x = 0.5, accounting for these discrepancies.

The ε_r and fitted $Q\times f$ values in the terahertz band are compared with those in the microwave band (approximately 12 GHz) in Fig. 7. Because ε_r in the terahertz band does not vary much with frequency, ε_r at 1 THz is chosen for comparison. For x = 0–0.3, the ε_r and $Q\times f$ values show similar trends in both frequency bands, increasing with x. Specifically, ε_r is greater in the microwave band than in the terahertz band, whereas the $Q\times f$ value is lower in the microwave band. This trend is attributed to the gradual withdrawal of certain polar phonon modes from the dielectric response as the frequency increases. However, when x = 0.4 and 0.5, the relationship between the dielectric properties in the two bands changes. ε_r in the terahertz band surpasses that in the microwave band, whereas the $Q\times f$ value in the terahertz band falls below that in the microwave band. Owing to the correlation in the dielectric properties between the terahertz and far-infrared bands [38], the far-infrared results measured and fitted are shown in Figs. S1 and S2 in the ESM. According to the new polar phonon mode peak highlighted in Fig. 6(d) and Figs. S1 and S2 in the ESM, the introduction of Ge^{4+} ions and the resulting crystal structural changes shift the original polar phonon modes to lower frequencies and introduce new polar phonon modes. Some polar phonon modes contribute little to the dielectric properties, such as the polar phonon mode at 1.87 THz and the polar phonon modes D and E in Figs. S1 and S2 in the ESM, whereas others contribute much to the dielectric properties, such as the polar phonon mode F, which increases ε_r and decreases the $Q\times f$ value in the terahertz band. This observation indicates that materials with excellent dielectric properties in the microwave band may not perform as well in the terahertz band, underscoring the need for further investigations to optimize materials for terahertz applications.

The following discussion focuses on the factors influencing the dielectric properties in the microwave band. Fig. 8(a) presents the measured ε_r, corrected permittivity (ε_{corr}), and theoretical permittivity (ε_{th}) of the MSGx ceramics. ε_{corr} is calculated via Eq. (8):

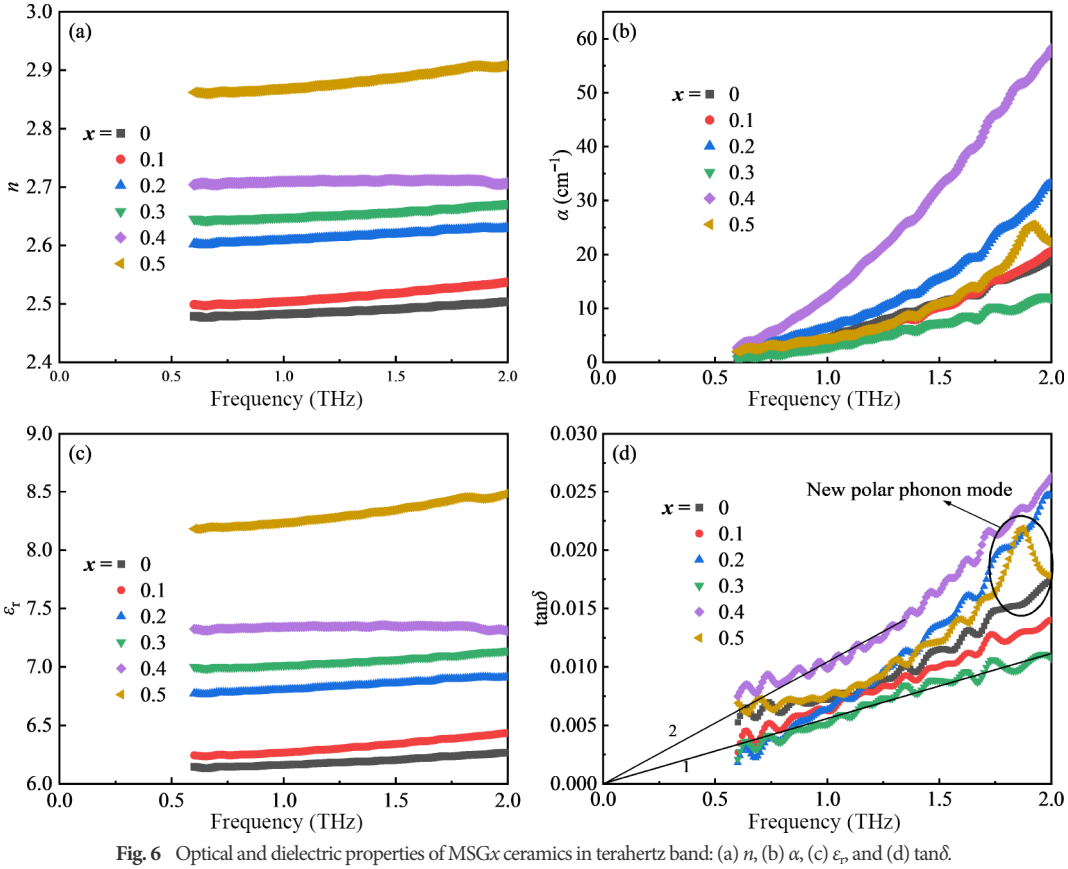

Fig. 6 Optical and dielectric properties of MSGx ceramics in terahertz band: (a) n, (b) α, (c) ε_r, and (d) tanδ.

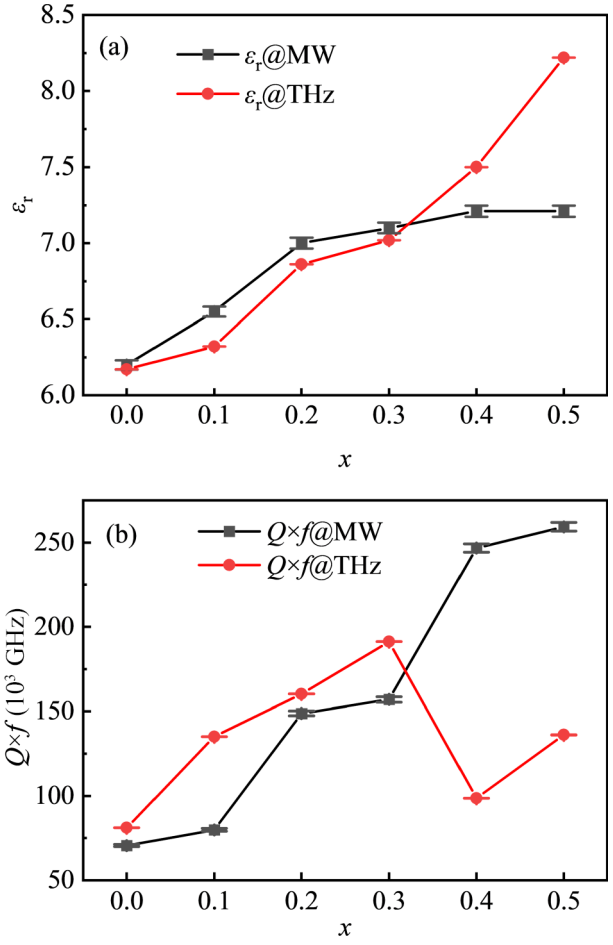

Fig. 7 Comparison of dielectric properties (a) ε_r and (b) $Q\times f$ values of MSGx ceramics in the microwave and terahertz bands.

$$\varepsilon_r = \varepsilon_{corr}\left[1 - \frac{3P(\varepsilon_{corr}-1)}{2\varepsilon_{corr}+1}\right] \quad (8)$$

where P is the porosity. ε_{th} is determined via the Clausius–Mossotti equation (Eq. (9)):

$$\frac{\varepsilon_r - 1}{\varepsilon_r + 2} = \frac{4\pi\alpha}{3V_m} \quad (9)$$

where V_m is the unit cell volume, and α represents the polarizability of the composition. Both ε_r and ε_{corr} increase with x and reach maximum values near x = 0.4 and 0.5, suggesting that porosity has a minimal impact on ε_r. ε_{th} increases monotonically with increasing x but remains consistently different from ε_{corr}. This discrepancy is due to the additional polarization mechanisms in silicate ceramics, particularly the "rattling space" effect, which was initially proposed by Shannon [39]. Notably, ε_{corr} is lower than ε_{th} when x = 0 and 0.1, whereas the magnitude relationship is reversed when $x \geq 0.2$. This indicates that the cations in the MSGx changed from "compressed" to "rattle" after the clino–ortho transition.

Figure 8(b) displays the experimental and calculated results of the $Q\times f$ value, the relative density (ρ_r), and the bond strain (ΔD_{strain}) for the MSGx ceramics. ΔD_{strain} is calculated from the distortion theorem of bond valence theory, as shown in the ESM, and represents the degree of distortion within the [Si/GeO_4] tetrahedron. Notably, the bond strain decreases significantly during the phase transition. This is due to the changes in I-beam units from "++−−" to "++ … " and in the [Si/GeO_4] tetrahedral

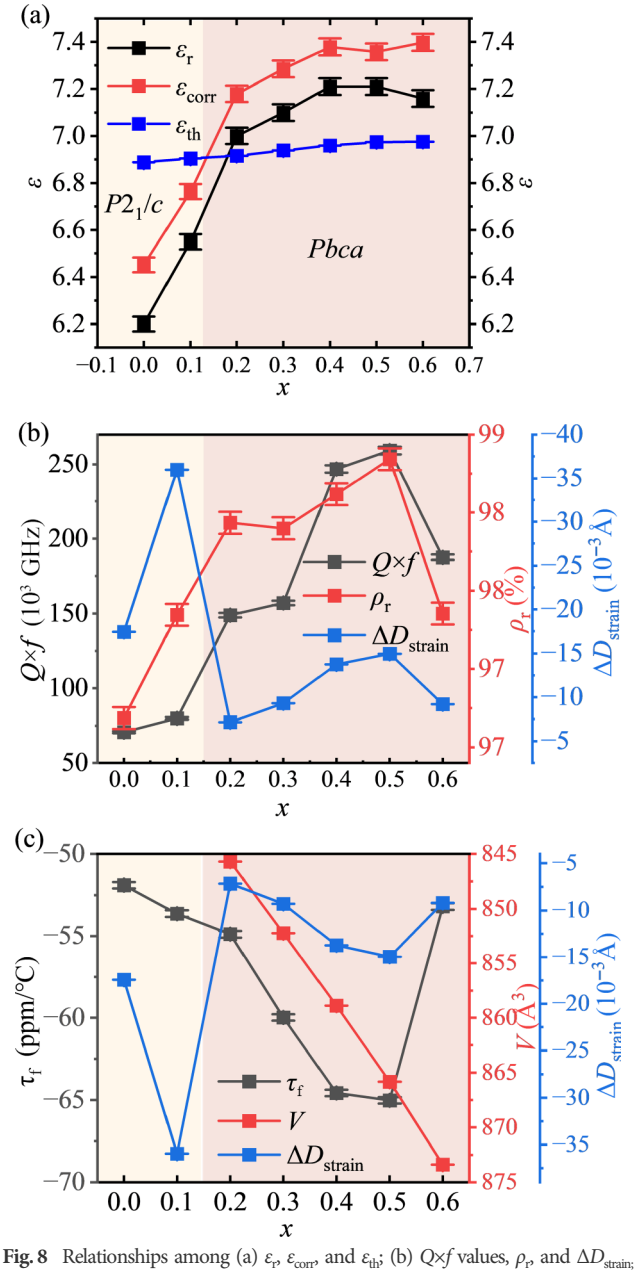

Fig. 8 Relationships among (a) ε_r, ε_{corr}, and ε_{th}; (b) $Q\times f$ values, ρ_r, and ΔD_{strain}; and (c) τ_f, V, and ΔD_{strain} of MSGx ceramics.

chains from the S configuration to the O configuration [34], resulting from Ge^{4+} substitution. The $Q\times f$ value increases stepwise from 70,600 (x = 0) to 148,800 (x = 0.2) across the clino-ortho phase transition, which is attributed to substantial changes in the bond strain. In the orthoenstituent phase, the $Q\times f$ value continues to increase with the addition of Ge^{4+} ions, reaching its peak at x = 0.5. As mentioned above in Figs. 5 and 6, the local distortion in the [Si/GeO_4] tetrahedral chains reaches its maximum at x = 0.5, and Fig. 8(b) shows that the distortion within the [Si/GeO_4] tetrahedron also reaches maximum values at x = 0.5. This finding indicates that lattice distortion not only induces a phase transition in the MSGx ceramics but also plays a crucial role in increasing the $Q\times f$ value in the chain silicates.

Figure 8(c) presents the τ_f, V, and ΔD_{strain} values of the MSGx ceramics. In general, τ_f is related to the temperature coefficient of permittivity (τ_ε) and the thermal expansion coefficient (α_l) as Eqs. (10) and (11) [40,41]:

$$\tau_f = -\left(\alpha_l + \frac{1}{2}\tau_\varepsilon\right),$$
$$\tau_\varepsilon = \frac{1}{\varepsilon}\left(\frac{\partial\varepsilon}{\partial T}\right)_P = \frac{(\varepsilon-1)(\varepsilon+2)}{\varepsilon}(A+B+C) \quad (10)$$
$$A = \frac{1}{3V}\left(\frac{\partial V}{\partial T}\right)_P, B = \frac{1}{3\alpha_m}\left(\frac{\partial \alpha_m}{\partial V}\right)_T\left(\frac{\partial V}{\partial T}\right)_P,$$
$$C = \frac{1}{3\alpha_m}\left(\frac{\partial \alpha_m}{\partial T}\right)_V \quad (11)$$

where A, B, and C represent the dilution of the concentration of dipoles caused by thermal expansion, the increase in polarizability due to volume expansion attributed to an increase in the "rattling space", and the direct dependence of the polarizability on temperature, respectively. α_l of microwave dielectric ceramics is typically approximately 10 ppm°·C^{-1}, and τ_ε is the main factor influencing τ_f [42]. Focusing on the orthoenstatite phase, the τ_f values of the ceramics exhibit trends similar to those of V and ΔD_{strain} when $x \le 0.5$, suggesting their joint influence. Specifically, both lattice expansion and increased distortion within the [Si/GeO$_4$] tetrahedron enhance the "rattling space" effect, resulting in an increase in τ_ε and consequently a decrease in τ_f.

Table 1 presents a comparison of the microwave dielectric properties in this work with those of other pyroxene ceramics, and the data are visualized in Fig. 9. $MgSi_{0.5}Ge_{0.5}O_3$ ceramics demonstrate the highest $Q\times f$ value in the microwave band among the silicate ceramics studied, except for glass-free Mg_2SiO_4 prepared with high-purity raw materials. The $Q\times f$ value of $MgSi_{0.7}Ge_{0.3}O_3$ ceramics in the terahertz band is superior, highlighting their strong potential for use in terahertz communication systems.

Table 1 Comparison of this work with reported pyroxene ceramics

Material	Sintering condition	ε_r	$Q\times f$ (GHz)	τ_f (ppm·°C^{-1})	Ref.
$MgSiO_3$	1380°C, 13 h	6.70	121,200	−17	[43]
$Mg_{0.85}Zn_{0.15}SiO_3$	1360°C, 9 h	8.05	138,500	−14	[25]
$Mg_{0.9}Ni_{0.1}SiO_3$	1425°C, 9 h	6.01	118,700	−10	[27]
$Mg_{0.9}Ca_{0.1}SiO_3$	1330°C, 2 h	8.01	47,500	−47	[24]
$Mg_{0.85}Co_{0.15}SiO_3$	1350°C, 9 h	8.11	145,846	−12	[26]
$CaMgSi_2O_6$	1300°C, 2 h	7.6	121,400	−66	[24]
$CaMg_{0.9}Zn_{0.1}Si_{1.9}Ge_{0.1}O_6$	1200°C, 4 h	7.46	191,100	−57.7	[15]
$CaCoSi_2O_6$	1175°C, 2 h	6.04	12,500	−18.91	[44]
$BaCuSi_2O_6$	1050°C, 3 h	8.45	31,400	0.36	[45]
$CaSiO_3$	1320°C, 2 h	6.69	25,300	—	[24]
$MgSi_{0.5}Ge_{0.5}O_3$	1400°C, 4 h	7.21	259,300	−65.02	This work

4 Conclusions

In this work, $MgSi_{1-x}Ge_xO_3$ (MSG$_x$, x = 0–0.6) ceramics were synthesized via the conventional solid-state method. All samples except those with x = 0.6 were sintered densely at 1400 °C. The MSGx ceramics display a phase transition from clinoenstatite at x = 0 and 0.1 to orthoenstatite at x = 0.2–0.5. This phase transition notably enhances the dielectric properties of the MSGx ceramics. For x = 0.6, a second phase of Mg_2SiO_4, together with pores, is generated due to the decreased chemical stability. The dielectric properties of the MSGx ceramics in both the microwave and terahertz bands exhibit similar trends when x = 0–0.3. However, for x > 0.3, ε_r in the terahertz band suddenly increases relative to that in the microwave band, and the $Q\times f$ value in the terahertz band correspondingly decreases. This arises from the shifting and emergence of polar phonon modes, which interfere with satisfying the condition $\omega \ll \omega_T$, resulting in increased ε_r and reduced $Q\times f$ values in the terahertz band. Excluding these effects, ε_r increases with x, influenced mainly by the cations changing from "compressed" to "rattle". The $Q\times f$ value and τ_f of the MSGx ceramics are inextricably linked to the lattice distortion. With respect to the $Q\times f$ value, the bond strain first decreases significantly during the phase transition due to the changes in I-beam units from "++−−" to "++ … " and in the [Si/GeO$_4$] tetrahedra chains from the S configuration to the O configuration. In orthoenstatite, local distortion in [Si/GeO$_4$] tetrahedral chains and the distortion within the [Si/GeO$_4$] tetrahedron play a significant role, maximizing the $Q\times f$ value at peak distortion when x = 0.5. Moreover, τ_f decreases with increasing V and ΔD_{strain}, both of which amplify the "rattling space" effect. These insights into the structure–property relationships pave the way for designing silicate ceramics with optimized $Q\times f$ values and near-zero τ_f values for advanced applications. The $MgSi_{0.5}Ge_{0.5}O_3$ ceramics exhibit superior microwave dielectric properties (ε_r = 7.21, $Q\times f$ = 259, 300 GHz), whereas the $MgSi_{0.7}Ge_{0.3}O_3$ ceramics excel in the terahertz band (ε_r = 7.02, $Q\times f$ = 191,300 GHz), establishing them as promising materials for future microwave and terahertz communication systems.

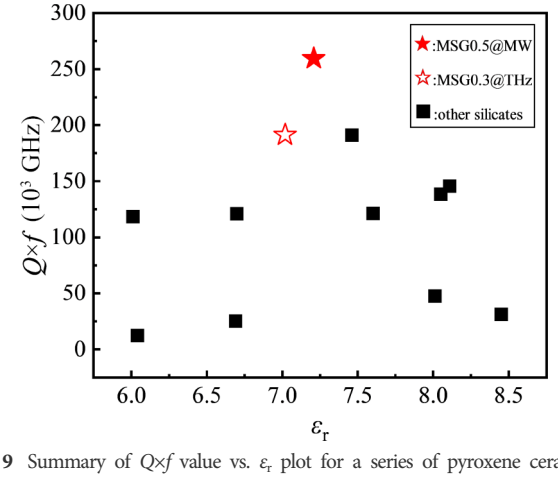

Fig. 9 Summary of $Q\times f$ value vs. ε_r plot for a series of pyroxene ceramics [15,24–27,43–45].

Acknowledgements

This work was supported by the National Natural Science

Foundation of China (Nos. 51872160 and U23A6014), the Shuimu Tsinghua Scholar Program of Tsinghua University (No. 2023SM245), and the Postdoctoral Fellowship Program of the China Postdoctoral Science Fund (No. GZC20240782).

Availability of data and materials

The data that support the findings of this study are available from the corresponding author upon reasonable request.

Competing interests

The authors have no competing interests to declare that are relevant to the content of this article.

Electronic Supplementary Material

Supplementary material is available in the online version of this article at https://doi.org/10.26599/JAC.2025.9221053.

References

[1] Xie M, Pajo JF, Awan MF, *et al.* Experimentation-as-a-service for validating 5G use cases in a large-scale 5G platform. In: Proceedings of the Joint European Conference on Networks and Communications & 6G Summit (EuCNC/6G Summit), 2024: 985–990.

[2] Zhan BR, Yu XC, Zeng ZJ, *et al.* China mobile network architecture for 6G. In: Proceedings of the 6GN for Future Wireless Networks, 2023: 100–117.

[3] Wang YF, Zhai JT, Wu ZP, *et al.* A THZ wireless link self-tracking technology. In: Proceedings of the 2nd International Conference on Electronic Information Engineering and Computer Communication (EIECC 2022), 2023: 331–336.

[4] Wang CX, You XH, Gao XQ, *et al.* On the road to 6G: Visions, requirements, key technologies, and testbeds. *IEEE Commun Surv Tutorials* 2023, **25**: 905–974.

[5] Raveendran A, Sebastian MT, Raman S. Applications of microwave materials: A review. *J Electron Mater* 2019, **48**: 2601–2634.

[6] Shehbaz M, Du C, Zhou D, *et al.* Recent progress in dielectric resonator antenna: Materials, designs, fabrications, and their performance. *Appl Phys Rev* 2023, **10**: 021303.

[7] Zhang YQ, Ogurtsov S, Vasilev V, *et al.* Advanced dielectric resonator antenna technology for 5G and 6G applications. *Sensors* 2024, **24**: 1413.

[8] Trabert JF, Humbla S, Müller J, *et al.* Microwave properties of low temperature co-fired ceramics for satellite communications and ultrawideband technologies. In: Proceedings of the 40th European Microwave Conference, 2010: 397–400.

[9] Vargas-Millalonco F, Martínez-Ledesma M, Reeves R, *et al.* Cryogenic characterization of LTCC material in millimeter-wave frequencies. *IEEE Trans Compon Packag Manufact Technol* 2024, **14**: 1007–1014.

[10] Kamutzki F, Schneider S, Barowski J, *et al.* Silicate dielectric ceramics for millimetre wave applications. *J Eur Ceram Soc* 2021, **41**: 3879–3894.

[11] Ohsato H, Tsunooka T, Sugiyama T, *et al.* Forsterite ceramics for millimeterwave dielectrics. *J Electroceram* 2006, **17**: 445–450.

[12] Nguyen NH, Lim JB, Nahm S, *et al.* Effect of Zn/Si ratio on the microstructural and microwave dielectric properties of Zn_2SiO_4 ceramics. *J Am Ceram Soc* 2007, **90**: 3127–3130.

[13] Huang FY, Su H, Li YX, *et al.* Low-temperature sintering and microwave dielectric properties of $CaMg_{1-x}Li_{2x}Si_2O_6$ (x = 0–0.3) ceramics. *J Adv Ceram* 2020, **9**: 471–480.

[14] Du K, Yin CZ, Yang JQ, *et al.* Crystal structure, far-infrared spectra, and microwave dielectric properties of bazirite-type $BaZr(Si_{1-x}Ge_x)_3O_9$ ceramics. *Ceram Int* 2022, **48**: 3592–3599.

[15] Lu YT, Guo WJ, Zhang CY, *et al.* Effects of Ge^{4+} substitution on the crystal structure and microwave/terahertz dielectric properties of diopside ceramics. *J Eur Ceram Soc* 2024, **44**: 5008–5015.

[16] Kamba S, Petzelt J, Buixaderas E, *et al.* High frequency dielectric properties of $A_5B_4O_{15}$ microwave ceramics. *J Appl Phys* 2001, **89**: 3900–3906.

[17] Yang HC, Zhang SR, Yang HY, *et al.* The latest process and challenges of microwave dielectric ceramics based on pseudo phase diagrams. *J Adv Ceram* 2021, **10**: 885–932.

[18] Ioachim A, Banciu MG, Toacsan MI, *et al.* Nickel-doped $(Zr_{0.8},Sn_{0.2})TiO_4$ for microwave and millimeter-wave applications. *Mater Sci Eng B* 2005, **118**: 205–209.

[19] Guo WJ, Lu YT, Ma ZY, *et al.* Defect-related broadband dielectric loss mechanisms of $Na_{1/2}Sm_{1/2}Ti_{1-z}(Al_{1/2}Nb_{1/2})_zO_3$ ceramics. *Acta Mater* 2023, **255**: 119093.

[20] Kanehara K, Urata S, Yasuhara S, *et al.* Dielectric property and polarization mechanism of sodium silicate glass in GHz–THz range. *Jpn J Appl Phys* 2022, **61**: SN1001.

[21] Choudhury N, Chaplot SL. Free energy and relative stability of the enstatite $Mg_2Si_2O_6$ polymorphs. *Solid State Commun* 2000, **114**: 127–132.

[22] Miyake A, Shimobayashi N, Kitamura M. Isosymmetric structural phase transition of orthoenstatite: Molecular dynamics simulation. *Am Mineral* 2004, **89**: 1667–1672.

[23] Hunt SA, Santangeli JR, Dobson DP, *et al.* Phase diagram and thermal expansion of orthopyroxene-, clinopyroxene-, and ilmenite-structured $MgGeO_3$. *Am Mineral* 2021, **106**: 1113–1127.

[24] Sun HP, Zhang QL, Yang H, *et al.* $(Ca_{1-x}Mg_x)SiO_3$: A low-permittivity microwave dielectric ceramic system. *Mater Sci Eng B* 2007, **138**: 46–50.

[25] Ullah A, Liu HX, Hao H, *et al.* Effect of Zn substitution on the sintering temperature and microwave dielectric properties of $MgSiO_3$-based ceramics. *Ceram Int* 2017, **43**: 484–490.

[26] Ullah A, Liu HX, Zhai PC, *et al.* Influence of Co substitution on the phase, microstructure, and microwave dielectric properties of $MgSiO_3$ ceramics. *J Mater Sci Mater Electron* 2019, **30**: 6469–6474.

[27] Ullah A, Liu HX, Hao H, *et al.* Phase and microstructure evaluation and microwave dielectric properties of $Mg_{1-x}Ni_xSiO_3$ ceramics. *J Electron Mater* 2016, **45**: 5133–5139.

[28] Welch MD, Pawley AR. Structural systematics of Ge substitution in primitive pyroxenes. *Phys Chem Miner* 2016, **43**: 161–169.

[29] Hakki BW, Coleman PD. A dielectric resonator method of measuring inductive capacities in the millimeter range. *IEEE Trans Microwave Theory Techn* 1960, **8**: 402–410.

[30] Courtney WE. Analysis and evaluation of a method of measuring the complex permittivity and permeability microwave insulators. *IEEE Trans Microwave Theory Techn* 1970, **18**: 476–485.

[31] Krupka J, Derzakowski K, Riddle B, *et al.* A dielectric resonator for measurements of complex permittivity of low loss dielectric materials as a function of temperature. *Meas Sci Technol* 1998, **9**: 1751–1756.

[32] Fu XJ, Guo YS, Zhou J. Terahertz optical parameters and lattice vibration-induced resonance of Er^{3+}-doped $Y_3Al_5O_{12}$ crystal. *J Electromagn Waves Appl* 2013, **27**: 1792–1799.

[33] Ruan XX, Chan CH. Terahertz free-space dielectric property measurements using time- and frequency-domain setups. *Int J RF Microw Comput Aided Eng* 2019, **29**: 21839.

[34] Cameron M, Papike JJ. Structural and chemical variations in pyroxenes. *Am Mineral* 1981, **66**: 1–50.

[35] Lambruschi E, Aliatis I, Mantovani L, *et al.* Raman spectroscopy of $CaM^{2+}Ge_2O_6$ (M^{2+} = Mg, Mn, Fe, Co, Ni, Zn) clinopyroxenes. *J Raman Spectrosc* 2015, **46**: 586–590.

[36] Flemming RL, Luth RW. ^{29}Si MAS NMR study of diopside–Ca-Tschermak clinopyroxenes: Detecting both tetrahedral and octahedral Al substitution. *Am Mineral* 2002, **87**: 25–36.

[37] Flemming RL, Terskikh V, Ye E. Aluminum environments in synthetic Ca-Tschermak clinopyroxene ($CaAlAlSiO_6$) from Rietveld

refinement, ^{27}Al NMR, and first-principles calculations. *Am Mineral* 2015, **100**: 2219–2230.

[38] Wang W, Wang X, Bao J, *et al*. Low-permittivity $BaCuSi_4O_{10}$-based dielectric ceramics: An available solution to connect low temperature cofired ceramic technology and millimeter-wave communications. *Chem Eng J* 2024, **494**: 153172.

[39] Shannon RD. Dielectric polarizabilities of ions in oxides and fluorides. *J Appl Phys* 1993, **73**: 348–366.

[40] Colla EL, Reaney IM, Setter N. Effect of structural changes in complex perovskites on the temperature coefficient of the relative permittivity. *J Appl Phys* 1993, **74**: 3414–3425.

[41] Yang Y, Fang WS, Lin HX, *et al*. $SrGa_{12}O_{19}$: The first low-ε_r Ga-based microwave dielectric ceramic with anomalous positive τ_f. *J Adv Ceram* 2024, **13**: 1432–1441.

[42] Lou Y, Wang W, Xu DM, *et al*. Effect of LiF and LBSCA glass on the microwave dielectric properties of $0.5BaCuSi_4O_{10}$–$0.5BaCuSi_2O_6$-based ceramics for LTCC applications. *J Am Ceram Soc* 2024, **107**: 6964–6973.

[43] Song ME, Kim JS, Joung MR, *et al*. Synthesis and microwave dielectric properties of $MgSiO_3$ ceramics. *J Am Ceram Soc* 2008, **91**: 2747–2750.

[44] Xiao M, Wei YS, Zhang P. The effect of sintering temperature on the crystal structure and microwave dielectric properties of $CaCoSi_2O_6$ ceramic. *Mater Chem Phys* 2019, **225**: 99–104.

[45] Song XQ, Lei W, Zhou YY, *et al*. Ultra-low fired fluoride composite microwave dielectric ceramics and their application for $BaCuSi_2O_6$-based LTCC. *J Am Ceram Soc* 2020, **103**: 1140–1148.